Optimal Hybrid Attitude Control for Detumbling Spacecraft

by

Emerson Vargas Niño

A thesis submitted in partial fulfillment for the
degree of Bachelor of Applied Science

in the
Department of Mechanical and Industrial Engineering
Faculty of Applied Science & Engineering
University of Toronto

Abstract

Department of Mechanical and Industrial Engineering
Faculty of Applied Science & Engineering
University of Toronto

Bachelor of Applied Science

by Emerson Vargas Niño

The B-Dot controller, a traditional method of detumbling is revisited and compared against a recently developed hybrid method which utilizes a magnetic-impulsive controller developed through modern optimal control theory in order to compensate for inherent uncontrollability found in purely magnetic control. A number of simulations were performed in order to compare the performance of the two systems over a range of conditions including differing orbital altitudes and methods for impulse application time.

Contents

List of Figures

List of Tables

Chapter 1

Introduction

1.1 Literature Review

A long popular technique for spacecraft attitude control has been through the use of static magnetorquers. These are multiple wire coil turns which induce a magnetic dipole moment when a control current passes through them, the interaction of the dipole moment and the Earth's magnetic field generates a torque which can be harnessed to control a spacecraft's attitude. There is a fundamental performance drawback in this system in which one axis will always be under actuated. This is a result of the torque being generated through the cross product interaction of the magnetic field and the magnetic dipole moment, as such there is no torque component parallel to the magnetic field [2]. This fundamental limitation has led to the rise of hybrid methods which combine more than one actuation method in order to make up for inherent uncontrollability. Among them, reaction wheels and magnetic actuators [3], magnetic and impulsive systems [2] [4], and Lorentz force and impulsive methods [5]. All of the studies above center on general spacecraft attitude control over time. In this work we will be discussing pure magnetic as well as magnetic-impulsive hybrid methods for the explicit purpose of detumbling. This mission critical scenario arises when a spacecraft has a large amount of angular momentum that it needs to dump quickly. Spacecraft in orbit regularly need to dump small quantities of momentum which accumulate over time due to external disturbances however they so when already in a stable orbit with all systems operational. Situations which require detumbling may also be situations in which not all systems are operational. Such is typically the case when a spacecraft is initially ejected from its launch vehicle and not all navigation sensors and actuation systems may be operational [6]. These conditions set apart detumbling as a specific area and application of spacecraft attitude control.

1.2 Thesis Outline

This work focuses spherically on a traditional, simplistic form of detumbling named the B-Dot law which is strictly magnetic and requires only the use of a readily available magnetometer. The second controller we will focus on is a hybrid optimal approach developed initially for formation flying utilizing Lorentz force actuation as well as impulsive control. This work was taken and extended to specifically target magnetic-impulsive hybrid systems. We will first develop the classic B-Dot controller explaining the theory behind its application with a discussion on the real life implications of implementing such a system. Following this we will develop optimal magnetic control as a stepping stone for optimal hybrid control, pausing to discuss the real world implications of an optimal magnetic controller. Finally, we extend optimal magnetic control to include the application of an impulsive thrust. We discuss how best to select the applied impulse timing and the implications of utilizing the presented hybrid system. Lastly we simulate a number of test cases for the controllers, comparing the performance of the systems over a range of conditions including differing orbital altitudes as well as differing methods for impulse application time.

Chapter 2

Orbital Mechanics

In order to understand the kinematics and dynamics of a spacecraft orbiting a body we must first describe and understand the setting itself. In this section we will describe the concepts of Orbital Mechanics necessary in order to fully describe an orbiting spacecraft.

2.1 Reference Frames

Given the nature of the problem at hand, it is apparent we need to be able to describe the rotation of the spacecraft around its center of mass and also the movement of the spacecraft with regards to the body it orbits. As such, we define a body-fixed reference frame $\mathcal{F}_B$ at the spacecraft center of mass and we apply the commonly used Geocentric Equatorial Coordinate System (GECS) [7] as our non-spinning inertial reference frame $\mathcal{F}_I$. The GECS has its origin at the center of the earth, an X-axis in the direction of the vernal equinox, the same as the direction of the constellation Aries, a Z-axis pointing towards the celestial north pole, directly above the geographic north pole, and a Y-axis which completes the coordinate system using a right-hand rule convention. Some key features mentioned of the co-ordinate system are shown in figure 2.1.

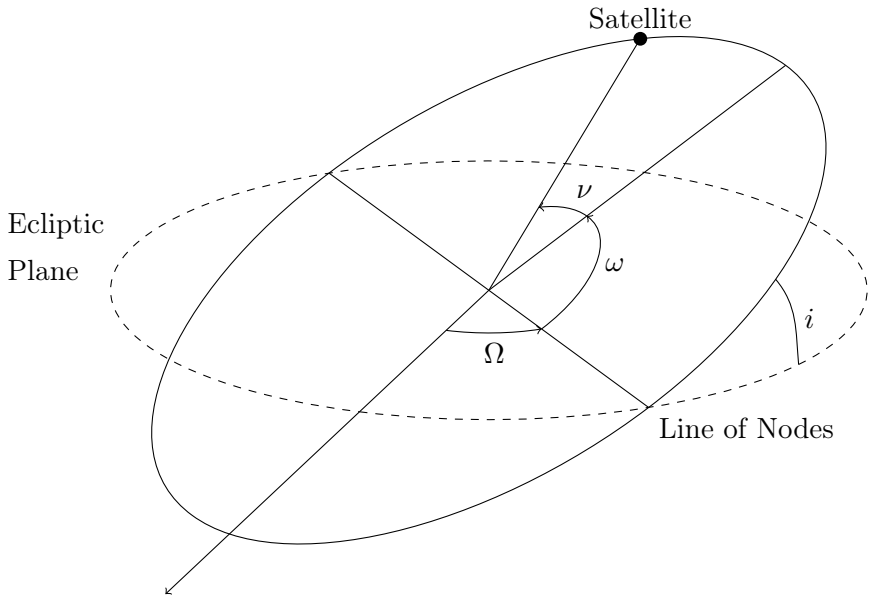

FIGURE 2.1: Key Orbital Parameters [1]

2.2 Orbital Model

We assume a circular orbit and in order to describe the location of the spacecraft in the inertial reference frame over time we define a position vector $\boldsymbol{r}_I(t)$ in the Cartesian coordinate system from the origin of $\mathcal{F}_I$ to the origin of $\mathcal{F}_B$ as follows,

$$\boldsymbol{r}_I(t) = \begin{bmatrix} X \\ Y \\ Z \end{bmatrix} = \begin{bmatrix} R\ cos(nt) \\ R\ sin(nt)cos(i) \\ R\ sin(nt)sin(i) \end{bmatrix} \tag{2.1}$$

where t is time, R the semi-major axis, i the inclination angle the orbit makes with respect to the equatorial plane, and n the mean motion of the satellite defined as

$$n = \sqrt{\frac{\mu}{R^3}} \tag{2.2}$$

with the standard gravitational parameter μ defined for earth.

Of primary focus will be a 450 km altitude spherical orbit at an inclination angle of 87° as well as a 1350 km altitude spherical orbit also at 87° shown modelled using equation 2.1 in figures 2.2 and 2.3 respectively.

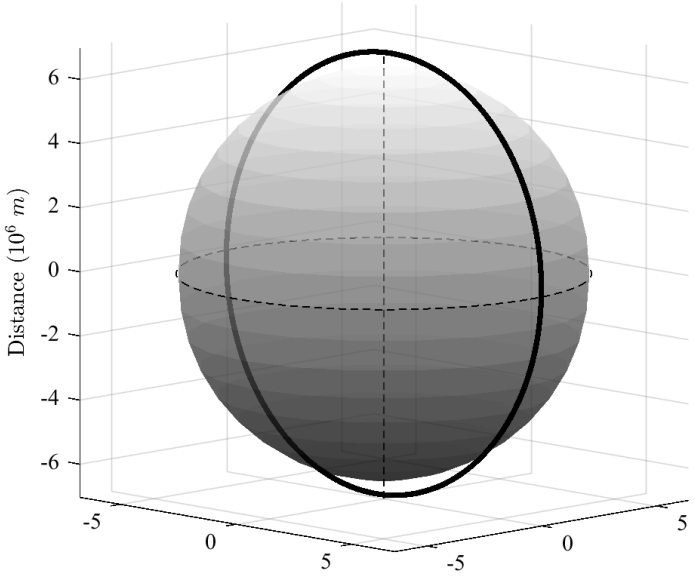

FIGURE 2.2: 450 km Altitude Spherical Orbit at 87°

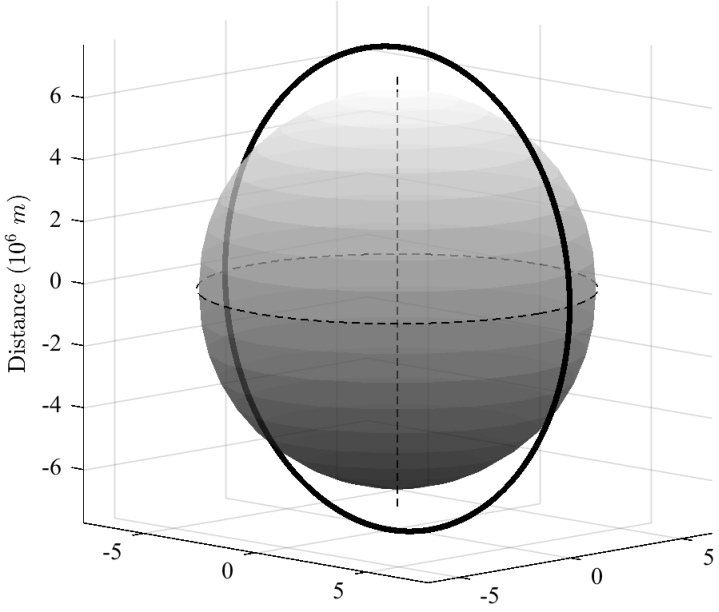

FIGURE 2.3: 1350 km Altitude Spherical Orbit at 87°

2.3 Magnetic Field Model

As the spacecraft will be rotating and translating as it orbits earth, the instantaneous magnetic field vector $\boldsymbol{B}$ in the spacecraft reference frame $\mathcal{F}_B$ will vary in time. A tilted dipole model is used to model the earth's geomagnetic field shown here in the Cartesian

coordinate system [8],

$$\boldsymbol{B}_I(t) = \frac{B_0}{R^5} \begin{bmatrix} 3XZ \\ 3YZ \\ 2Z^2 - X^2 - Y^2 \end{bmatrix} \tag{2.3}$$

Where the XYZ coordinates in time are obtained from 2.1 and B_0 is equal to the magnetic moment of the Earth [9].

Earth's magnetic field tends to vary more towards the poles, hence small spacecraft which take advantage of the earth's magnetic field tend to prefer a near polar orbit where both the magnitude and variability of the magnetic field and is larger. This can be seen clearly in figures 2.4 and 2.5 which model the magnetic field, using equation 2.3, at 87° and 30° respectively.

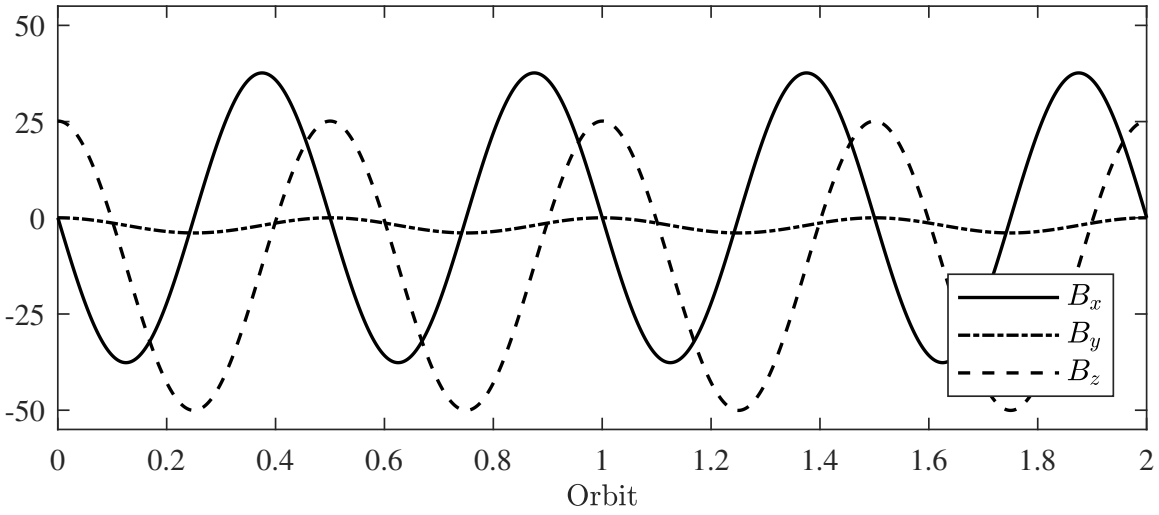

FIGURE 2.4: Earth Magnetic Field Components at 87° Inclination

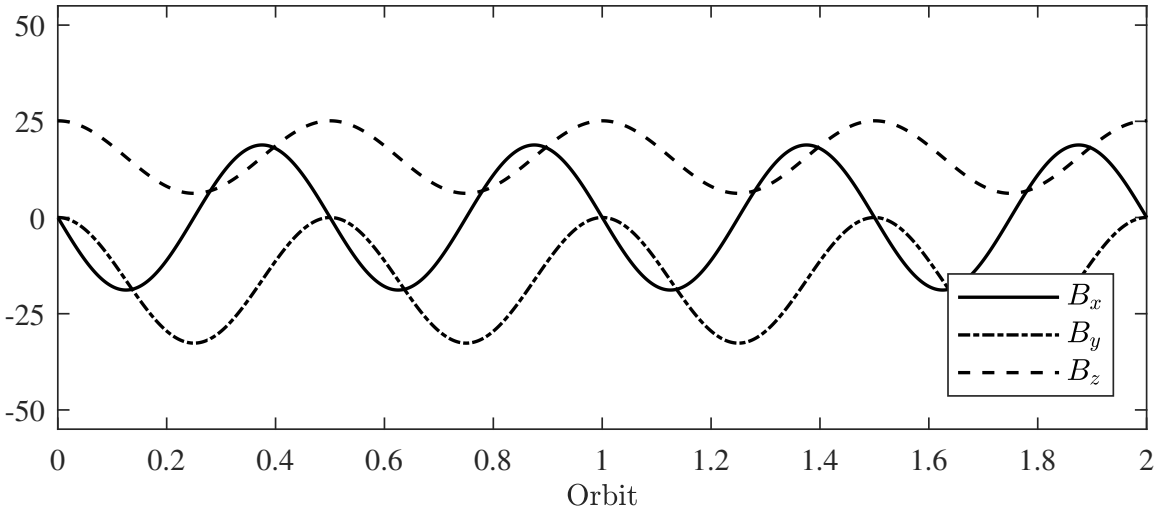

FIGURE 2.5: Earth Magnetic Field Components at 30° Inclination

Chapter 3

Spacecraft Kinematics and Dynamics

In order to undergo a study of spacecraft control it is important to first understand the laws that govern the movement of spacecraft in the vacuum of space. Kinematics serves to describe motion and dynamics serves to describe motion considering underlying forces.

3.1 Kinematics

3.1.1 Rotational Kinematics

Two common ways of describing the rotation of rigid bodies in space include Euler Angles, and Quaternions. Euler Angles use 3 parameters ϕ, θ, ψ in order to describe what is commonly referred to as yaw, pitch and roll. Quaternions use a set of 4 parameters $\boldsymbol{\epsilon} = [\ \epsilon_1 \quad \epsilon_2 \quad \epsilon_3\ ]^T$ and η, which satisfy the orthogonality constraint $\boldsymbol{\epsilon}^T\boldsymbol{\epsilon} + \eta^2 = \mathbf{1}$, where $\mathbf{1}$ is the identity matrix. Quaternions, unlike Euler Angles are free of singularities and are thus preferred [10].

Angular velocity and quaternion rates of change can be related through the following equation which fully describes the rotational kinematics of the spacecraft [11].

$$\begin{bmatrix} \dot{\boldsymbol{\epsilon}} \\ \dot{\eta} \end{bmatrix} = \frac{1}{2} \begin{bmatrix} \eta \mathbf{1}_{3\times 3} + \boldsymbol{\epsilon}^{\times} \\ -\boldsymbol{\epsilon}^T \end{bmatrix} \boldsymbol{\omega} \tag{3.1}$$

The skew-symmetric operator $(\cdot)^\times$ used in equation 3.1 is used to represent the cross product operator and acts on a generic vector $\boldsymbol{a}_{n\times 1}$ to create a skew-symmetric matrix which satisfies the condition $\boldsymbol{a}^{\times T} = -\boldsymbol{a}^\times$, such that

$$\boldsymbol{a}^\times = \begin{bmatrix} 0 & -a_3 & a_2 \\ a_3 & 0 & -a_1 \\ -a_2 & a_1 & 0 \end{bmatrix} \tag{3.2}$$

3.1.2 Rotation Matrix

In order to express a parameter from the inertial frame in the body-fixed frame we can apply the rotation matrix formulated with Quaternions as [10],

$$\boldsymbol{C}_{BI} = (\eta^2 - \boldsymbol{\epsilon}^T\boldsymbol{\epsilon})\mathbf{1} + 2\boldsymbol{\epsilon}\boldsymbol{\epsilon}^T - 2\eta\boldsymbol{\epsilon}^\times \tag{3.3}$$

3.2 Dynamics

3.2.1 Rotational Dynamics

The rotational dynamics of a spacecraft can be modelled using Euler's equation of motion [11],

$$\boldsymbol{I}\dot{\boldsymbol{\omega}} + \boldsymbol{\omega}^\times\boldsymbol{I}\boldsymbol{\omega} = \boldsymbol{\tau}_{ctrl} + \boldsymbol{\tau}_{dist} \tag{3.4}$$

Where $\boldsymbol{I}$ is the inertia matrix, and $\boldsymbol{\omega}$ refers to the angular velocity in the body-fixed reference frame. The first torque contribution $\boldsymbol{\tau}_{ctrl}$, represents the torque intentionally applied to the spacecraft for the purpose of attitude control and the second contribution $\boldsymbol{\tau}_{dist}$ represents the unintentional external torque disturbances. Both torque contributions are modelled as being applied about the spacecraft's center of mass.

3.2.2 External Torques

3.2.2.1 Control Torques

As stated in chapter 1, for the purposes of detumbling control, the spacecraft modelled in this study utilizes a combination of a 3 axis propulsion system and 3 magnetorquers on

each of the spacecraft's principal inertia axis. The torque applied by these two systems is modeled as follows [2],

$$\boldsymbol{\tau}_{ctrl} = \boldsymbol{\tau}_{mag} + \boldsymbol{\tau}_{imp} \tag{3.5}$$

where,

$$\boldsymbol{\tau}_{mag} = \boldsymbol{m}^{\times}\boldsymbol{B}_B \tag{3.6}$$

$$\boldsymbol{\tau}_{imp} = \sum_{k=1}^{N-1} \boldsymbol{n}_k \delta(t - t_k) \tag{3.7}$$

The first control torque term $\boldsymbol{\tau}_{mag}$ in equation 3.5 refers to the magnetic torque caused by the interaction of the earth's magnetic field, in the body-fixed reference frame, and the magnetic dipole moment induced by passing a controlled current through multiple wire coil turns within a magnetorquer body.

As seen by the application of the skew-symmetric operator to the magnetic dipole moment in equation 3.6, the resulting torque will always be orthogonal to the instantaneous magnetic field vector. As such, the axis parallel to the instantaneous magnetic field vector will always be uncontrollable. Due to the orientation of the earth's magnetic field, an orbiting spacecraft would thus temporarily lose control over one axis as it crosses over the polar regions, and would lose temporarily lose control of a separate axis over the Equatorial regions [12]. A complimentary torque system may be positioned and actuated in such as way as to compensate for this lack of control.

Some common torque systems implemented in spacecraft in addition to magnetorquers include reaction wheels, and different types of thrusters such as resistojets, monopropulsion systems, hall thrusters, and cold gas thrusters to name a few [13]. The spacecraft in this study utilizes a generic impulsive thruster in order to compensate for the uncontrollability of the magnetorquers.

The thruster control torque contribution is seen in equation 3.7, and is modelled as an impulse using the Dirac-Delta function δ, applied a total of $N-1$ times at differing time intervals.

3.2.2.2 Distburbance Torques

The second contribution of torque $\boldsymbol{\tau}_{dist}$ in equation 3.4 comes from external disturbances such as aerodynamic drag, gravity gradient, residual magnetic dipoles from onboard electronics, and solar pressure. For near-earth small spacecraft the most prominent

sources of disturbance come from the gravity gradient, and residual magnetic dipoles from onboard electronics. These contributions can be respectively modelled as [4],

$$\boldsymbol{\tau}_{dist} = \frac{3\mu}{|\boldsymbol{r}_B|^5}\boldsymbol{r}_B^{\times}\boldsymbol{I}\boldsymbol{r}_B + \boldsymbol{m}_{dist}^{\times}\boldsymbol{B}_B \tag{3.8}$$

As the focus of this study is primarily controller design and comparison we elect to not model these disturbances however it should be noted that depending on the altitude of the orbit the spacecraft inhabits, they may or may not be negligible.

Chapter 4

Magnetic Attitude Control

For the purposes of attitude control the spacecraft being modelled has three orthogonal magnetorquers and a propulsion impulse system. The effect of the magnetorquers can be modelled using equation 3.6. The design parameter in this equation is m, the magnetic dipole moment. We now look at two models for selecting m, a B-Dot controller and an optimal approach.

4.1 Magnetic Control

Considering only the kinetic component of the Hamiltonian describing the spacecraft, and modelling the kinetic energy as strictly rotational we arrive at [14]

$$T = \frac{1}{2}\boldsymbol{\omega}^T \boldsymbol{I}\boldsymbol{\omega} \tag{4.1}$$

The rate of change of the rotational kinetic energy is then given as

$$\dot{T} = \boldsymbol{\omega}^T \boldsymbol{I}\dot{\boldsymbol{\omega}} \tag{4.2}$$

Considering Euler's equation of motion 3.4 with external torque provided by magnetics alone 3.6 we get

$$\boldsymbol{I}\dot{\boldsymbol{\omega}} + \boldsymbol{\omega}^{\times}\boldsymbol{I}\boldsymbol{\omega} = \boldsymbol{m}^{\times}\boldsymbol{B}_B \tag{4.3}$$

Substituting this into equation 4.2 we arrive at

$$\dot{T} = \boldsymbol{\omega}^T(-\boldsymbol{\omega}^{\times}\boldsymbol{I}\boldsymbol{\omega} + \boldsymbol{m}^{\times}\boldsymbol{B}_B) \tag{4.4}$$

After simplifying this form we arrive at

$$\dot{T} = -k \left(\boldsymbol{B}_B^{\times} \, \boldsymbol{\omega} \right)^T \boldsymbol{B}_B^{\times} \, \boldsymbol{\omega} \tag{4.5}$$

Equation 4.5 is significant as $\dot{T} \leq 0$, leading to the conclusion that the feedback $\boldsymbol{B}_B^{\times} \, \boldsymbol{\omega}$ effectively reduces the rotational kinetic energy of the system.

When implemented practically, the feedback above requires the measurement of both the magnetic field as well as the angular velocity through the use of a magnetometer and a gyroscope respectively.

Detumbling is the act of dissipating a typically large amount of angular momentum from a spacecraft. This typically occurs after the spacecraft is initially ejected from its launch vehicle, when any external disturbances perturb the spacecraft significantly, and when the spacecraft's main active controller does not respond for whatever reason. All aforementioned scenarios are critical and non-nominal, in addition it is reasonable to assume not all spacecraft systems are online and operational in the above conditions. As such special care must be taken when selecting the detumbling method in order to minimize risk of failure. [6]

When taking the aforementioned statements into consideration, it becomes clear that a detumbling controller that requires the use of two separate sensors in order to operate is highly impractical and could risk mission failure. We now turn to the B-Dot controller which avoids the aforementioned problem and is a popular choice for detumbling spacecraft due to its simplicity and ease of implementation.

4.2 B-Dot Controller

The relationship between the magnetic field rate of change in $\mathcal{F}_I$ and $\mathcal{F}_B$ can be modeled as [14]

$$\dot{\boldsymbol{B}}_I = \dot{\boldsymbol{B}}_B \; + \boldsymbol{\omega} \times \boldsymbol{B}_B \tag{4.6}$$

As seen from $\mathcal{F}_B$, there are two contributions that cause the magnetic field to vary over time. The first contribution is a result of the spacecraft travels in an orbit around earth, thus its position relative to the origin of $\mathcal{F}_I$ changes over time varying the inertial magnetic field vector from equation 2.3; the timescale of this change has an order of magnitude of hours. The second contribution is a result of the spacecraft rotating about its center of mass, the origin of $\mathcal{F}_B$, thus the instantaneous magnetic field experienced by

the spacecraft changes in time; the timescale of this change has an order of magnitude of seconds.

Because of the slow rate of change of the first contribution, we can effectively neglect this term. Rearranging and reducing equation 4.6 results in [14]

$$\dot{\boldsymbol{B}}_B \approx \boldsymbol{B}_B^{\times}\, \boldsymbol{\omega} \tag{4.7}$$

Hence we can see that that the local magnetic field rate of change provides a meaningful value for the attitude rate of the satellite, a requirement of the previously discussed feedback for the magnetic controller in equation 4.5. This is significant as this new requirement can be approximated trivially through the use of a readily available on-board magnetometer by differentiating between two successive sensor readings as,

$$\dot{\boldsymbol{B}}_B \approx \frac{\boldsymbol{B}_B(t_n) - \boldsymbol{B}_B(t_{n-1})}{t_n - t_{n-1}} \tag{4.8}$$

Multiplying the above result by a constant negative gain results in the B-Dot controller,

$$\boldsymbol{m} = -\boldsymbol{k}\dot{\boldsymbol{B}}_B \tag{4.9}$$

Substituting back into equation 3.6, we obtain an expression for the torque of a B-Dot controller

$$\boldsymbol{\tau}_{mag} = \left(-\boldsymbol{k}\dot{\boldsymbol{B}}_B\right)^{\times} \boldsymbol{B}_B \tag{4.10}$$

4.2.1 Controller Benefits and Limitations

B-Dot controllers have proven popular over the years as they only require a magnetometer and magnetorquers be present. Magnetometers are relatively inexpensive sensors which can easily be made redundant and magnetorquers are mechanically simpler than their complicated mechanical or chemical counterpart systems such as reaction wheels or propulsion systems respectively [6].

These controllers however are not without fault and they do have performance limitations. The approximation set out in equation 4.7 hold best when the rate of change of the body-fixed magnetic field $\dot{\boldsymbol{B}}_B$ varies more rapidly as a result of the spacecraft motion than the spacecraft orbit [14]. As this is always the case in the detumbling scenarios outlined above we can confidently use B-Dot for detumbling purposes. As with any method requiring an approximation however, there will always be an inherent error

present. We further discuss the efficacy of B-Dot in chapter 6. Next we examine a more robust magnetic controller which aims to maximize performance.

4.3 Optimal Magnetic Control

4.3.1 Linearization

Designing controllers for nonlinear systems can lead to unnecessary complexities and should be avoided if possible. Recalling that equation 3.4, used to describing the dynamics of the spacecraft, is non-linear we now linearize it in preparation for the optimal controller design.

We assume $\mathcal{F}_I$ and $\mathcal{F}_B$ differ by a small angle transformation. Since for small angles every attitude parameterization method, including Quaternions and Euler Angles, is approximately equal we can assume that [11]

$$\boldsymbol{\theta} \approx 2\boldsymbol{\epsilon} \tag{4.11}$$

This leads to a rotation matrix given by

$$\boldsymbol{C}_{BI} \approx \mathbf{1} - \boldsymbol{\theta}^{\times} \tag{4.12}$$

Furthermore, if we assume the spacecraft's angular rates are small then

$$\dot{\boldsymbol{\theta}} \approx \boldsymbol{\omega} \tag{4.13}$$

Substituting the aforementioned relationship into equation 3.4 while considering only the magnetic torque contribution from equation 3.6 and neglecting the products of small terms, results in the following linearized equation of motion [3]

$$\boldsymbol{I}\ddot{\boldsymbol{\theta}} = -\boldsymbol{B}_I^{\times}\boldsymbol{m} \tag{4.14}$$

It should be noted that the magnetic torque in the linearized equation uses the inertial reference frame $\mathcal{F}_I$ instead of the proper body-fixed frame $\mathcal{F}_B$ as applying the transformation [11]

$$\boldsymbol{B}_B = \boldsymbol{C}_{BI}\boldsymbol{B}_I \approx (\mathbf{1} - \boldsymbol{\theta}^{\times})\boldsymbol{B}_I \tag{4.15}$$

and making the same assumptions as before, as well as neglecting small terms results in

$$\boldsymbol{B}_B \approx \boldsymbol{B}_I \tag{4.16}$$

These simplifications allow the controller to be designed around linear equations however practically, when implemented into the spacecraft it is only logical to use $\boldsymbol{B}_B$ as this is what is readily available through sensor measurements.

4.3.2 State Space Model

The dynamics of an optimal control law for a continuous magnetic input can be modelled for the linear time-varying (LTV) case as [3]

$$\dot{\boldsymbol{x}}(t) = \boldsymbol{A}\boldsymbol{x}(t) + \boldsymbol{B}(t)\boldsymbol{u}(t) \tag{4.17}$$

Where $\dot{\boldsymbol{x}}$ is the differentiated state vector, $\boldsymbol{A}$ the state matrix, $\boldsymbol{u}$ the continuous control input and $\boldsymbol{B}$ the continuous control input matrix, not to be confused with the magnetic field vector. We define the state vector as

$$\boldsymbol{x} = \begin{bmatrix} \boldsymbol{\theta} \\ \dot{\boldsymbol{\theta}} \end{bmatrix} \tag{4.18}$$

We now implement the differentiated form of 4.18 along with the linear equation of motion 4.14 into the state space model resulting in the LTV equation [3]

$$\begin{bmatrix} \dot{\boldsymbol{\theta}}(t) \\ \ddot{\boldsymbol{\theta}}(t) \end{bmatrix} = \begin{bmatrix} \mathbf{0}_{3\times3} & \mathbf{1}_{3\times3} \\ \mathbf{0}_{3\times3} & \mathbf{0}_{3\times3} \end{bmatrix} \begin{bmatrix} \boldsymbol{\theta}(t) \\ \dot{\boldsymbol{\theta}}(t) \end{bmatrix} + \begin{bmatrix} \mathbf{0}_{3\times3} \\ -\boldsymbol{I}^{-1}\boldsymbol{B}_I^{\times}(t) \end{bmatrix} \boldsymbol{m}(t) \tag{4.19}$$

4.3.3 Linear-Quadratic Regulator

In order to minimize the effort of the continuous control input $\boldsymbol{u}$ for the continuous LTV system in 4.17, we define a quadratic cost function $\boldsymbol{\mathcal{J}}$ given by [3]

$$\boldsymbol{\mathcal{J}} = \frac{1}{2}\boldsymbol{x}^T(t_f)\boldsymbol{S}\boldsymbol{x}(t_f) + \frac{1}{2}\int_0^{t_f} \left[\boldsymbol{x}^T(t)\boldsymbol{Q}\boldsymbol{x}(t) + \boldsymbol{u}^T(t)\boldsymbol{R}\boldsymbol{u}(t)\right] dt \tag{4.20}$$

Where $\boldsymbol{x}$ and $\boldsymbol{u}$ are from equation 4.17. $\boldsymbol{Q}$, $\boldsymbol{R}$ and $\boldsymbol{S}$ are symmetric positive definite matrices, with $\boldsymbol{Q}$ and $\boldsymbol{R}$ being used to weigh the state and control effort relative importance.

The combination of the linear system dynamics in 4.17 as well as the quadratic cost function in 4.20 results in the well known linear-quadratic regulator (LQR) problem.

Utilizing the Hamiltonian associated with the model, as well as the calculus of variations as outlined in [2], results in the optimal continuous feedback control law which minimizes the cost function [3]

$$\boldsymbol{u} = -\boldsymbol{R}^{-1}\boldsymbol{B}^{T}(t)\boldsymbol{P}(t)\boldsymbol{x}(t) \tag{4.21}$$

As well as the following Riccati equation [3]

$$-\dot{\boldsymbol{P}}(t) = \boldsymbol{A}^{T}\boldsymbol{P}(t) + \boldsymbol{P}(t)\boldsymbol{A} - \boldsymbol{B}(t)\boldsymbol{P}(t)\boldsymbol{R}^{-1}\boldsymbol{P}(t)\boldsymbol{B}^{T}(t) + \boldsymbol{Q} \tag{4.22}$$

The Riccati equation is peculiar in that it must be integrated backwards in time from $\boldsymbol{P}(t_f)$ to $\boldsymbol{P}(0)$ using the terminal condition $\boldsymbol{P}(t_f) = \boldsymbol{0}_{3\times3}$.

The coefficients of 4.21 and 4.22 are given as part of 4.17 and 4.20.

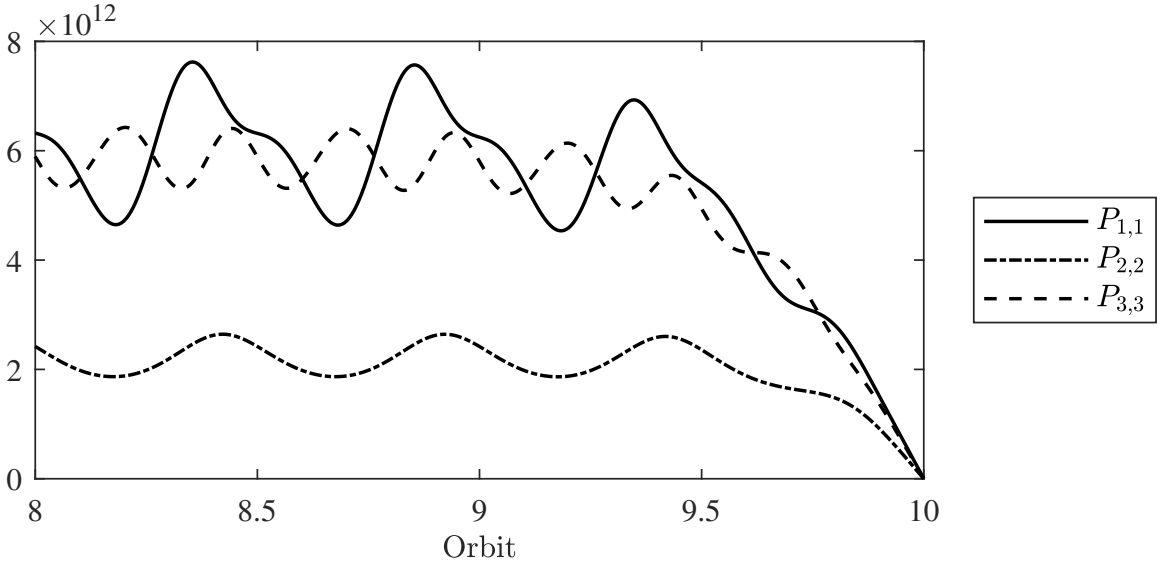

FIGURE 4.1: Continous Riccati Solution, Diagonal Components

4.3.4 Optimal Magnetic Controller

As the magnetic dipole moment $\boldsymbol{m}$ is the continuous control input $\boldsymbol{u}$, we thus obtain an optimal solution for the time-varying magnetic dipole moment. Simplifying and formatting the relevant variables as a gain matrix we obtain the optimal magnetic controller

$$\begin{aligned} \boldsymbol{m} &= -\boldsymbol{K}\boldsymbol{\omega} \\ &= -\left[\boldsymbol{R}^{-1}(-\boldsymbol{I}^{-1}\boldsymbol{B}_{I}^{\times})^{T}\boldsymbol{P}\right]\boldsymbol{\omega} \end{aligned} \tag{4.23}$$

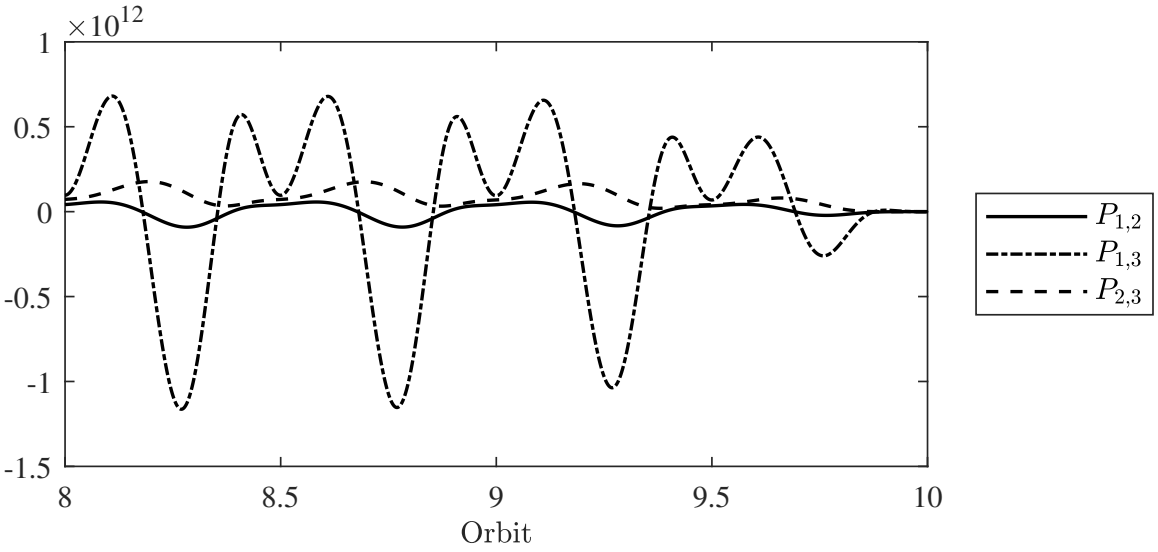

FIGURE 4.2: Continous Riccati Solution, Non-Diagonal Components

Substituting back into equation 3.6, we obtain an expression for the torque of a B-Dot controller [3]

$$\boldsymbol{\tau}_{mag} = \left(-\left[\boldsymbol{R}^{-1}(-\boldsymbol{I}^{-1}\boldsymbol{B}_I^{\times})^T\boldsymbol{P}\right]\boldsymbol{\omega}\right)^{\times}\boldsymbol{B}_B \tag{4.24}$$

4.3.5 Controller Benefits and Limitations

The optimal magnetic controller introduces a more robust method for selecting the magnetic dipole moment based on optimal control theory. The obvious practical downside of this method is the requirement of both angular velocity and magnetic field measurements. The requirement for the Riccati equation solution is not a serious drawback as the solution can be computed ahead of time and stored as a compact text file on the spacecraft. It is recommended to store the full solution of the Riccati and not an approximation as this could lead to performance degradation [5]. A performance comparison of the optimal magnetic and B-Dot controller is carried out in chapter 6.

Chapter 5

Hybrid Optimal Control

There are a number of inherent limitations associated with control provided exclusively by magnetorquers [4] that ultimately result in a magnetorquer based system not being robust enough to be the main active controller. In a detumbling use case however such limitations can often be overlooked, however one may wish to increase the performance of the magnetorquer based system during periods of low efficiency. In this chapter we will discuss the hybrid controller method introduced in [5] which utilizes both magnetorquers and impulsive thrusters for the purpose of complimenting the magnetic controller during periods it is least efficient. The optimal hybrid controller leverages the optimal magnetic control discussed in section 4.3 introducing the impulsive component of control.

5.1 State Space Model

The introduction of discrete system dynamics as a result of the thruster's impulsive nature lead us introduce a new state space model for this behavior as well as clarify the continuous state space model of the magnetic actuators outlined in equation 4.17. We can model the hybrid system as follows

$$\dot{\boldsymbol{x}}(t) = \boldsymbol{A}_c\boldsymbol{x}(t) + \boldsymbol{B}_c(t)\boldsymbol{u}_c(t), \qquad t \neq t_k \tag{5.1}$$

$$\boldsymbol{x}(t_k^+) = \boldsymbol{A}_d\boldsymbol{x}(t_k^-) + \boldsymbol{B}_d\boldsymbol{v}_d, \qquad t = t_k \tag{5.2}$$

Equations 5.1 and 5.2 correspond to the continuous and discrete models respectively and thus use corresponding $(\cdot)_c$ and $(\cdot)_d$ subscripts to denote variables associated with the two models.

Impulses are applied at time instance t_k, with t_k^- and t_k^+ denoting the instant immediately before and after the impulse application.

We linearize the equation of motion considering only the impulsive torque contribution, making the appropriate substitutions and simplifications as outlined in subsection 4.3.1 and substitute this into equation 5.2 resulting in the explicit hybrid state space model [4]

$$\begin{bmatrix} \dot{\boldsymbol{\theta}}(t) \\ \ddot{\boldsymbol{\theta}}(t) \end{bmatrix} = \begin{bmatrix} \mathbf{0}_{3\times3} & \mathbf{1}_{3\times3} \\ \mathbf{0}_{3\times3} & \mathbf{0}_{3\times3} \end{bmatrix} \begin{bmatrix} \boldsymbol{\theta}(t) \\ \dot{\boldsymbol{\theta}}(t) \end{bmatrix} + \begin{bmatrix} \mathbf{0}_{3\times3} \\ -\boldsymbol{I}^{-1}\boldsymbol{B}_I^{\times}(t) \end{bmatrix} \boldsymbol{m}(t), \qquad t \neq t_k \tag{5.3}$$

$$\begin{bmatrix} \boldsymbol{\theta}(t_k^+) \\ \dot{\boldsymbol{\theta}}(t_k^+) \end{bmatrix} = \begin{bmatrix} \mathbf{1}_{3\times3} & \mathbf{0}_{3\times3} \\ \mathbf{0}_{3\times3} & \mathbf{1}_{3\times3} \end{bmatrix} \begin{bmatrix} \boldsymbol{\theta}(t_k^-) \\ \dot{\boldsymbol{\theta}}(t_k^-) \end{bmatrix} + \begin{bmatrix} \mathbf{0}_{3\times3} \\ -\boldsymbol{I}^{-1} \end{bmatrix} \boldsymbol{n}_k, \qquad t = t_k \tag{5.4}$$

5.2 Linear-Quadratic Regulator

The quadratic cost function associated with the hybrid system is given as [3]

$$\boldsymbol{\mathcal{J}} = \frac{1}{2}\boldsymbol{x}^T(t_f)\boldsymbol{S}\boldsymbol{x}(t_f) + \frac{1}{2}\int_0^{t_f} \left[\boldsymbol{x}^T(t)\boldsymbol{Q}_c\boldsymbol{x}(t) + \boldsymbol{u}^T(t)\boldsymbol{R}_c\boldsymbol{u}(t)\right] dt \tag{5.5}$$

$$+ \frac{1}{2}\sum_{N}^{k=1} \left[\boldsymbol{x}^T(t_k^-)\boldsymbol{Q}_d\boldsymbol{x}(t_k^-) + \boldsymbol{v}^T\boldsymbol{R}_d\boldsymbol{v}\right] \tag{5.6}$$

The weight matrices $\boldsymbol{Q_c}$, $\boldsymbol{Q_d}$, $\boldsymbol{R_c}$, $\boldsymbol{R_d}$ are all symmetric positive definite matrices, with $\boldsymbol{Q}$ and $\boldsymbol{R}$ matrices responsible for weighing state and control effort relative importance for both continuous and discrete states, depending on the respective subscript.

Utilizing the continuous and discrete Hamiltonians associated with the model, as well as the calculus of variations as outlined in [3], results in the optimal continuous and discrete feedback control laws which minimize the hybrid cost function

$$\boldsymbol{u} = -\boldsymbol{R}_c^{-1}\boldsymbol{B}_c^T(t)\boldsymbol{P}(t)\boldsymbol{x}(t), \qquad t \neq t_k \tag{5.7}$$

$$\boldsymbol{v}_k = -\boldsymbol{R}_d^{-1}\boldsymbol{B}_d^T\boldsymbol{A}_d^{-T}\left[\boldsymbol{P}(t_k^-) - \boldsymbol{Q}_d\right]\boldsymbol{x}(t_k^-), \qquad t = t_k \tag{5.8}$$

As well as the following continous and discrete Riccati equations respectively [4]

$$-\dot{\boldsymbol{P}}(t) = \boldsymbol{A}_c^T\boldsymbol{P}(t) + \boldsymbol{P}(t)\boldsymbol{A}_c - \boldsymbol{B}_c(t)\boldsymbol{P}(t)\boldsymbol{R}_c^{-1}\boldsymbol{P}(t)\boldsymbol{B}_c^T(t) + \boldsymbol{Q}_c \tag{5.9}$$

$$\boldsymbol{P}(t_k^-) = \boldsymbol{Q}_d + \boldsymbol{A}_d^T\boldsymbol{P}(t_k^+)\boldsymbol{A}_d - \boldsymbol{A}_d^T\boldsymbol{P}(t_k^+)\boldsymbol{B}_d\left(\boldsymbol{R}_d + \boldsymbol{B}_d^T\boldsymbol{P}(t_k^+)\boldsymbol{B}_d\right)^{-1}\boldsymbol{B}_d^T\boldsymbol{P}(t_k^+)\boldsymbol{A}_d \tag{5.10}$$

For the hybrid problem at hand the Riccati equation must be integrated backwards in time from the time t_f to t_k^+ using the terminal condition $\boldsymbol{P}(t_f) = \mathbf{0}_{3\times3}$. The thrusters impulsive behavior render the continuous form of the Riccati undefined at the instance of impulse application t_k, thus at t_k^+ the discrete Riccati 5.10 must be applied to obtain $P(t_k^-)$ at which point the continuous Riccati can resume being applied until the subsequent impulse application.

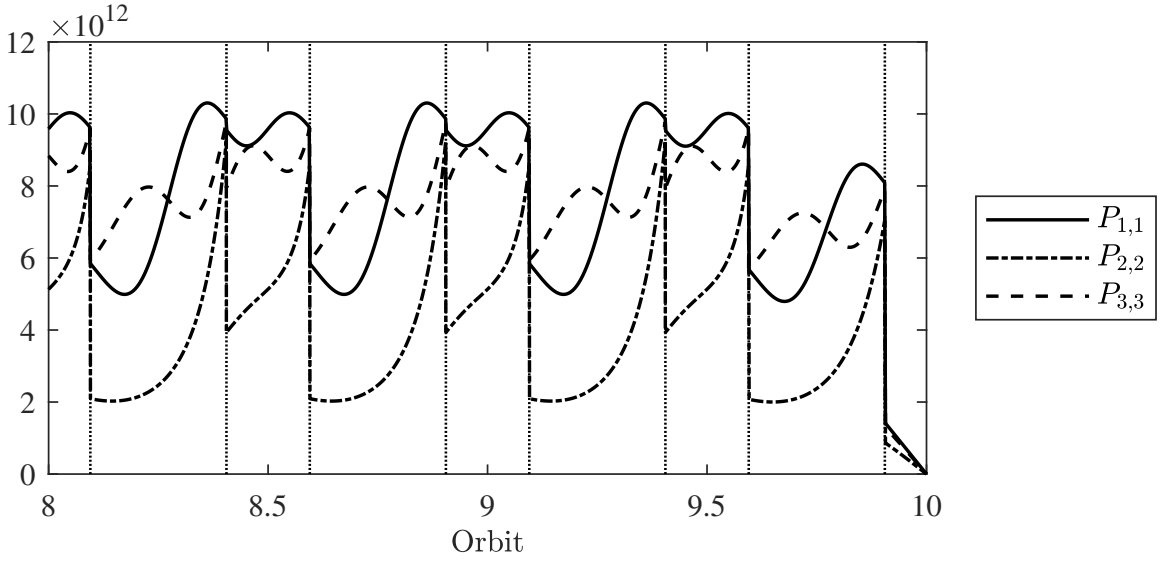

FIGURE 5.1: Discontinuous Riccati Solution, Diagonal Components

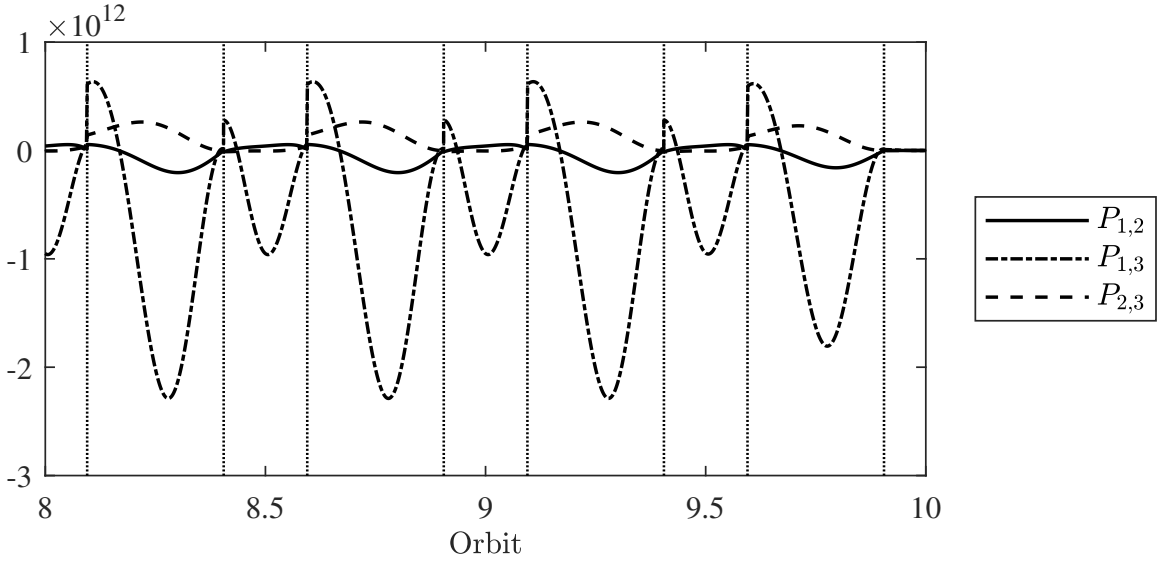

FIGURE 5.2: Discontinuous Riccati Solution, Non-Diagonal Components

5.3 Optimal Impulse Time Selection

Given the discrete nature of impulsive thruster systems, a natural problem that arises with their use is the selection of optimal application times. The majority of methods utilize some measure of system controllability often provided through the controllability Gramian. The controllability Gramian can be found as the solution of the Lyapunov equation, which is ever present in discussions of spacecraft control theory as magnetic control laws often rely on Lyapunov stability or Floquet theory [15]. The controllability Gramian is given by [5]

$$\boldsymbol{W}_c = \int_{t_0}^{t_1} e^{\boldsymbol{A}(t-\tau)} \boldsymbol{B}\boldsymbol{B}^T e^{\boldsymbol{A}^T(t-\tau)} d\tau \tag{5.11}$$

Where $\boldsymbol{A}$ and $\boldsymbol{B}$ are the coefficients to our continuous state space model 4.17. For an LTV system such as this the controllability Gramian must be computed over small time steps h spanning from t_0 through to t_f.

The controllability Gramian can determine if the system is controllable and the level of controllability. A system is controllable from t_0 to t_1 if $\boldsymbol{W}_c$ is non-singular. An $n \times n$ square matrix such as $\boldsymbol{W}_c$ is non-singular only if its rank is equal to n, otherwise known as having full-rank, or equivalently if the determinant of the system is non-zero [5]. The interpretation of this requirement is that the all rows and columns are linearly independent and invertible. We determine the rank of $\boldsymbol{W}_c$ and ascertain the system is controllable. It's worth noting that in a hybrid system such as this, if a large enough gain is applied to the impulsive thrusters system, the system will be controllable regardless of the magnetic field [11].

The interpretation of $\boldsymbol{W}_c$ is that it defines an ellipsoid located in the system state space which encompasses the set of states reachable within a singular unit of energy[16]. The eigenvalues of the system quantify the energy required to reach a particular state and the closer to zero a particular eigenvalue is, the closer to singular $\boldsymbol{W}_c$ will be, thus the minimum energy necessary to drive the system to a particular state will be higher[16]. As such, we use the minimum eigenvalue as a metric for least controllable state present in the state space system representation, which in our case models the magnetic control. This technique tell us when magnetic control is least effective, therefore it is only logical that additional control effort at this instant, provided by thrusters in this scenario, should lead to increased momentum dampening. This technique has proven effective in hybrid attitude controllers for spacecraft [5] [2].

In figure 5.3 we see the three eigenvalues associated with our particular system and see the first eigenvalue is always smaller than the other two. Analyzing this eigenvalue

more closely in figure 5.4, we find the time instances associated with the system's local minima and choose these to be our impulse application times. The associated locations in orbit can be seen in figure 5.5. Only the first and second impulse locations are marked as we will mostly be looking at two impulse application systems. A discussion of the effect of a third impulse application can be found in subsection 6.2.2, and a discussion of the performance benefits associated with this optimal impulse application time over arbitrarily chosen application times can be found in subsection 6.2.2.

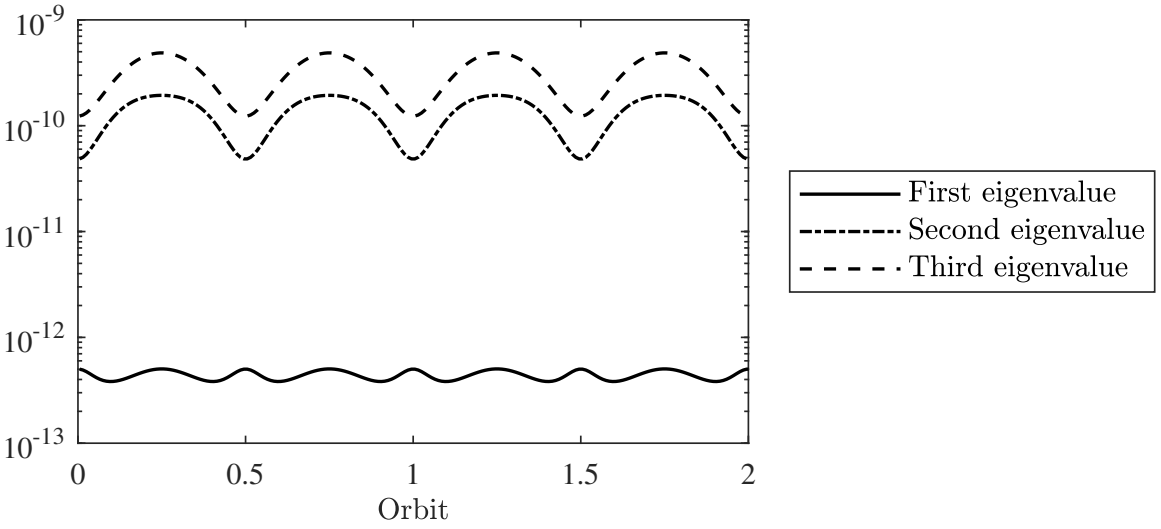

FIGURE 5.3: Eigenvalues of the Controllability Gramian Matrix

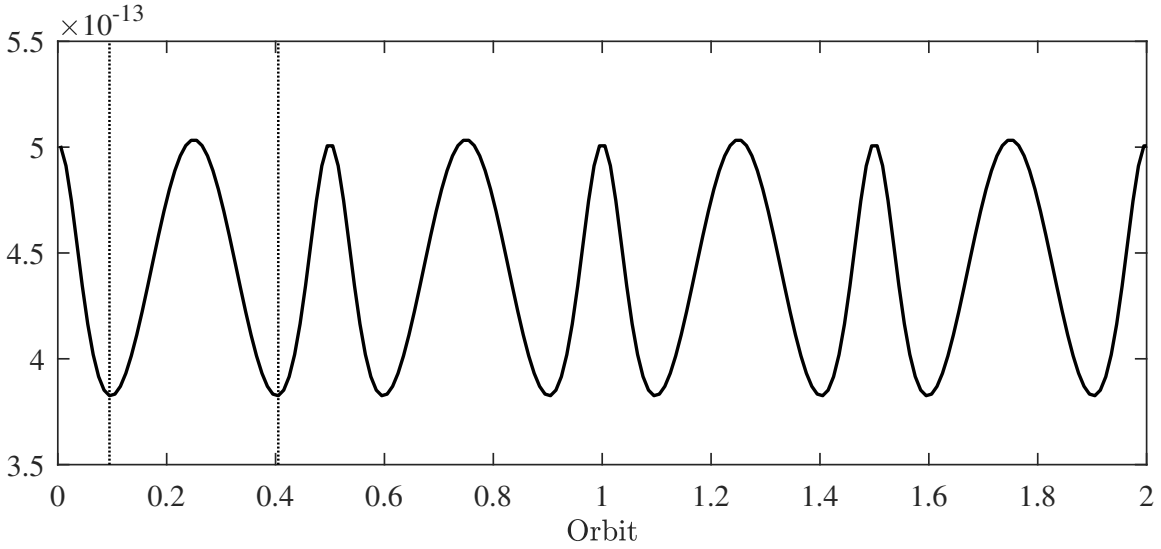

FIGURE 5.4: First Eigenvalue of the Controllability Gramian Matrix

5.4 Hybrid Optimal Controller

As the hybrid controller does not modify the continuous portion of the controller, the application of the continuous control will be the same as outlined in section 4.3. In

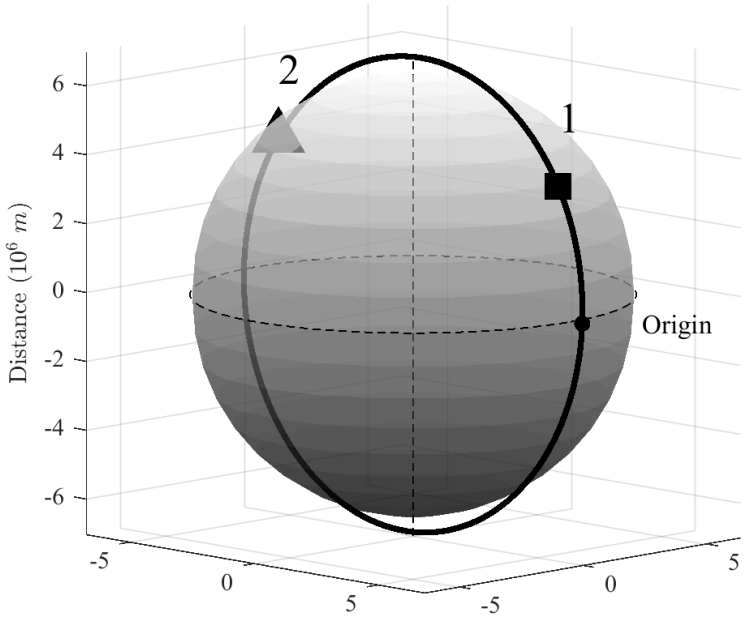

FIGURE 5.5: Location of Two Optimally Placed Thruster Instances

order to apply the impulsive control however, the impulsive feedback control must be calculated using 5.8 and fed into 5.2 to determine the change in spacecraft attitude.

5.4.1 Controller Benefits and Limitations

Every controller we have looked at so far is increasingly complicated as compared to the last. The optimal hybrid controller, an extension of the optimal magnetic controller, is the most complex controller discussed because of the necessity for thrusters. As with any system, the higher the number of components, the higher the risk of failure. This would imply however that the spacecraft does not already include thrusters, which many spacecraft do. Having a propulsion system on-board as well as magnetorquers means that should the spacecraft require detumbling, and all systems are operational, The optimal hybrid control can be utilized in order to detumble the spacecraft at a much higher rate than would otherwise be possible utilizing magnetics alone. The performance benefit of this controller over those previously discussed is investigated in chapter 6.

Chapter 6

Simulation Results

6.1 Simulation Setup

With our description of the orbital path from equation 2.1, geomagnetic field from equation 2.3, and spacecraft kinematics and dynamics from equation 3.4 and 3.1 respectively, we now have a complete description of the physics of the system which we implement into MATLAB. Equations 3.4 and 3.1 are integrated simultaneously over time in order to describe the spacecraft's changes in attitude. A 4^{th} order Runge-Kutta scheme (RK4) with a fixed step size h was chosen for integration for its simplicity and sufficiently low error. In big O notation, a fixed step RK4 scheme has $\mathcal{O}(5)$ error over a single step size and has a total error of $\mathcal{O}(4)$ over the entire interval $[a, b]$ [17].

Unless otherwise noted all simulations have a 450 km orbit with a near polar 87° inclination angle. The hybrid controllers apply two impulses as seen in 5.5.

The attitude initial conditions were given by

$$\begin{aligned} \boldsymbol{\epsilon}_0 &= [\ 0 \quad 0 \quad 0 \quad 0\ ]^T,\ \eta_0 = 1 \\ \boldsymbol{\omega}_0 &= [\ 0.05236 \quad 0.05236 \quad 0.05236\ ]^T\ rad/s \end{aligned} \tag{6.1}$$

Where 0.05236 rad/s [18] corresponds to experimental values of a similarly sized spacecraft in LEO being ejected from its launch vehicle, and thus needing to be detumbled.

In addition,

$$\boldsymbol{I} = \begin{bmatrix} 27 & 0 & 0 \\ 0 & 17 & 0 \\ 0 & 0 & 25 \end{bmatrix} kg\ m^2 \tag{6.2}$$

In order to simplify choosing controller inputs for the state space models, well known diagonal matrices were multiplied by scalar values such that

$$\begin{aligned} \boldsymbol{Q}_c &= q_c \ \boldsymbol{I} = 10^8 \ \boldsymbol{I} \\ \boldsymbol{Q}_d &= q_d \ \boldsymbol{I} = 10^{10} \ \boldsymbol{I} \\ \boldsymbol{R}_c &= r_c \ \mathbf{1}_{3\times3} = 1.5 \times 10^4 \ \mathbf{1}_{3\times3} \\ \boldsymbol{R_d} &= r_d \ \mathbf{1}_{3\times3} = 10^{13} \ \mathbf{1}_{3\times3} \end{aligned} \tag{6.3}$$

In order to quantitatively compare simulation results, the following norms were defined to act as performance metrics

$$\begin{aligned} ||\boldsymbol{\omega}||_{3T} &= \sqrt{\frac{1}{3T}\int_0^{3T} \boldsymbol{\omega}^T\boldsymbol{\omega} dt]]} \\ ||\boldsymbol{m}||_{3T} &= \sqrt{\frac{1}{3T}\int_0^{3T} \boldsymbol{m}^T\boldsymbol{m} dt} \end{aligned} \tag{6.4}$$

In order quantify the electrical energy consumed by the magnetorquers, a representative study was used which models a similarly sized spacecraft with the same orbit. The energy consumption is then given as [2]

$$E = \left[3R/(n^2A^2)\right] \int_0^T \boldsymbol{m}^T\boldsymbol{m} dt \tag{6.5}$$

where R is the coil's electrical resistance, n the number of coil turns, A the coil's total area. The product of $\left[3R/(n^2A^2)\right]$ was calculated as 3.03×10^5 based on representative missions [2].

6.2 Simulation Discussion

6.2.1 B-Dot and Hybrid Controller

Shown in figure 6.1 are the results of a nominal simulation using a B-Dot controller, while figure 6.2 shows the results of an optimal hybrid controller. Immediately apparent upon inspection is that the hybrid controller is able to detumble the spacecraft not only faster, but ultimately also to a greater degree as the angular velocity components appear to be closer to 0 at the 2 orbit mark. Despite this however, the B-Dot controller is still able to effectively damp out oscillations within the 2 orbit window. The B-Dot controller effectively takes twice as long as the hybrid control to approach the same degree of

dampening (as seen at the 1 orbit mark of 6.1). The solution to the Riccati equation associated with the hybrid controller is seen in figure 6.3 and 6.4.

The performance metrics from table 6.1 show that the hybrid controller is still heavily dependent on the magnetic portion of the control as the magnetic moment between optimal and B-Dot is very close. Both magnetic and impulsive components are clearly evenly balanced. Worth noting is the fact that the second thruster instance does not appear to be strictly necessary as the angular velocity components were nearly 0.

TABLE 6.1: Performance Metrics for B-dot And Hybrid Controllers At Nominal Conditions

Figure	**Controller**	$\|\|\boldsymbol{\omega}\|\|$ $(\frac{rad}{s})$	$\|\|\boldsymbol{m}\|\|$ (Am^2)	**E** (GJ)
6.1	B-Dot	0.085	3.0	46.4
6.2	Hybrid	0.069	2.7	36.6

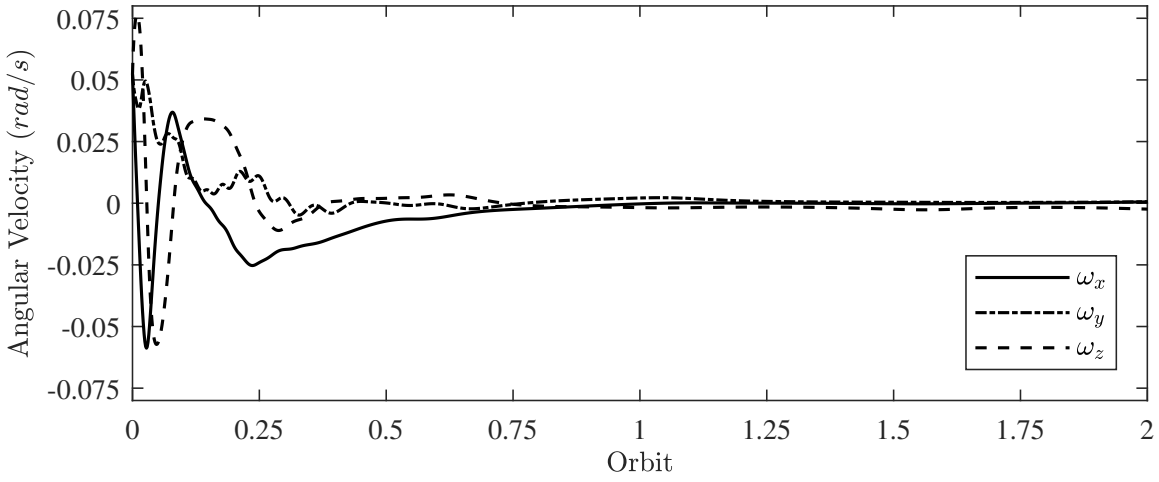

FIGURE 6.1: B-Dot Controller at Nominal Conditions

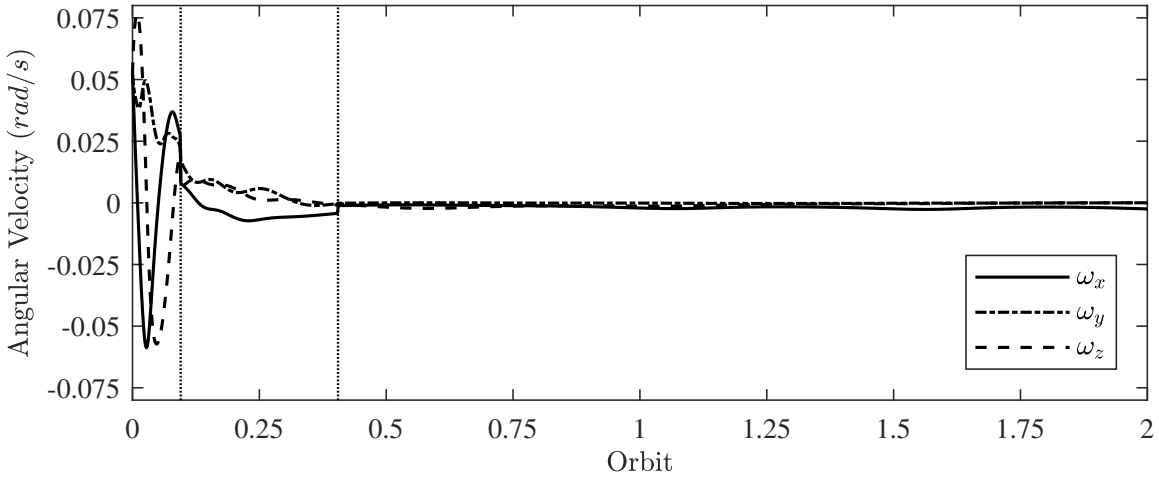

FIGURE 6.2: Hybrid Controller at Nominal Conditions

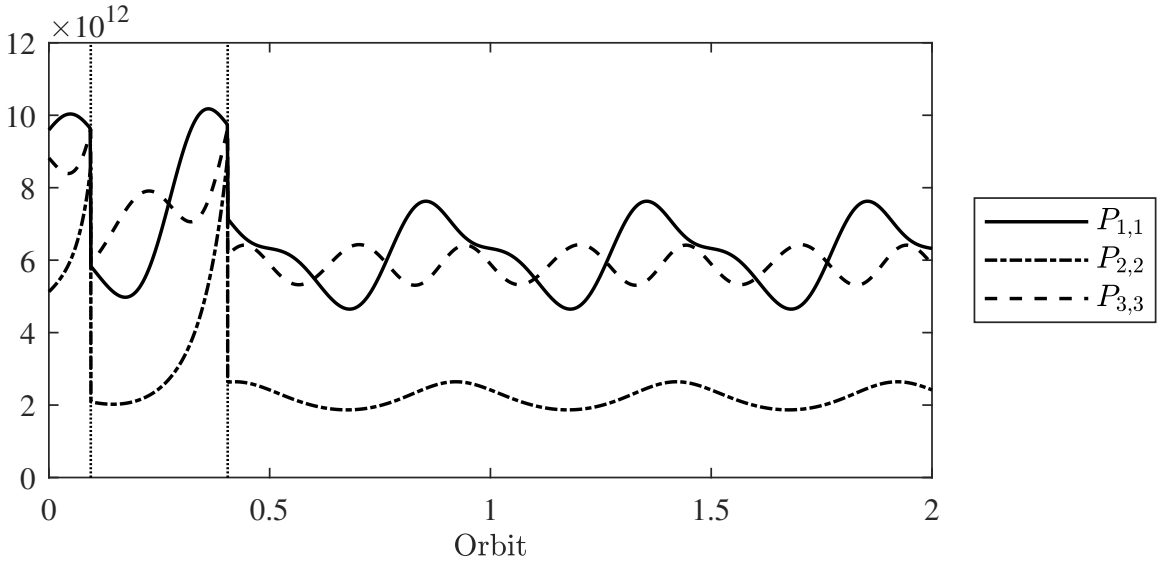

FIGURE 6.3: Riccati Solution for 2 Impulses, Diagonal Components

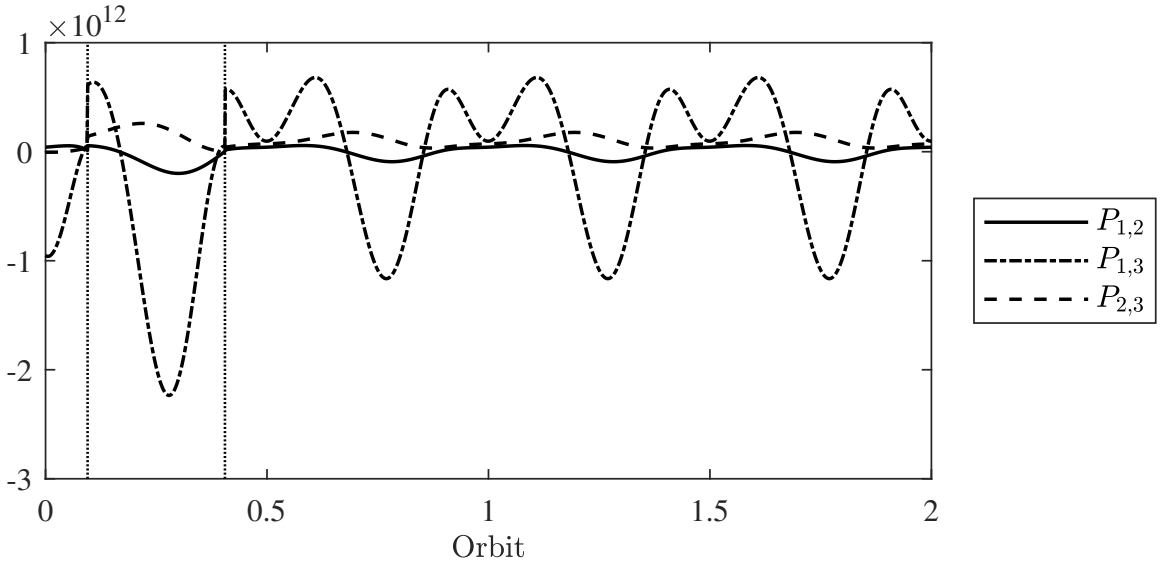

FIGURE 6.4: Riccati Solution for 2 Impulses, Off-Diagonal Components

6.2.2 Thrust Variation

The effect of a secondary thruster instance does not appear to have much of an effect for optimally placed thruster instances as well as arbitrarily placed thruster instances as seen in figures 6.2 and 6.7 respectively. This is because a single thruster instance combined with he magnetic control is able to effectively detumble the space fact before the arrival of the secondary optimal thruster instance. This is significant as it leads to the conclusion that the optimal thruster instance selection through the minimum eigenvalue as discussed in section 5.3, is not strictly necessary, although can provide marginal improvements as seen by the modest increase in performance by the angular

velocity performance metric of table 6.2. The table also reveals that the performance benefits of three optimally placed thruster instances as opposed to two, is practically null as seen in figure 6.5, reinforcing the design decision to analyze the effect of only two thruster instances.

TABLE 6.2: Performance Metrics for Hybrid Controller With Differing Thruster Instances

Figure	**Controller**	**Impulses**	$\|\|\boldsymbol{\omega}\|\|$ $(\frac{rad}{s})$	$\|\|\boldsymbol{m}\|\|$ (Am^2)	**E** (GJ)
6.2	Hybrid	2 nominal	0.069	2.7	36.6
6.5	Hybrid	3 nominal	0.069	2.7	36.6
6.7	Hybrid	2 arbitrary	0.077	2.8	40.4

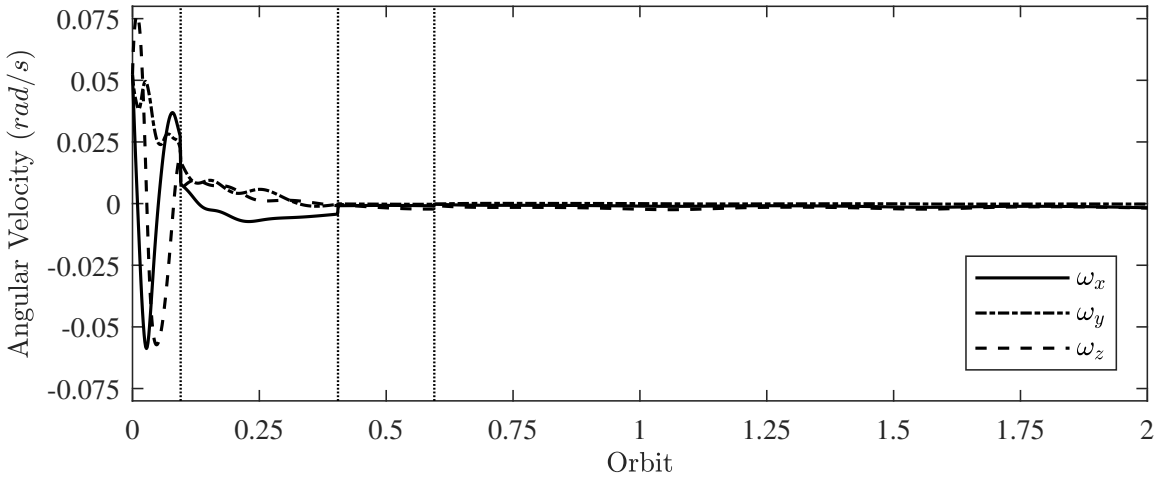

FIGURE 6.5: Hybrid Controller Utilizing 3 Optimally Placed Thruster Instances

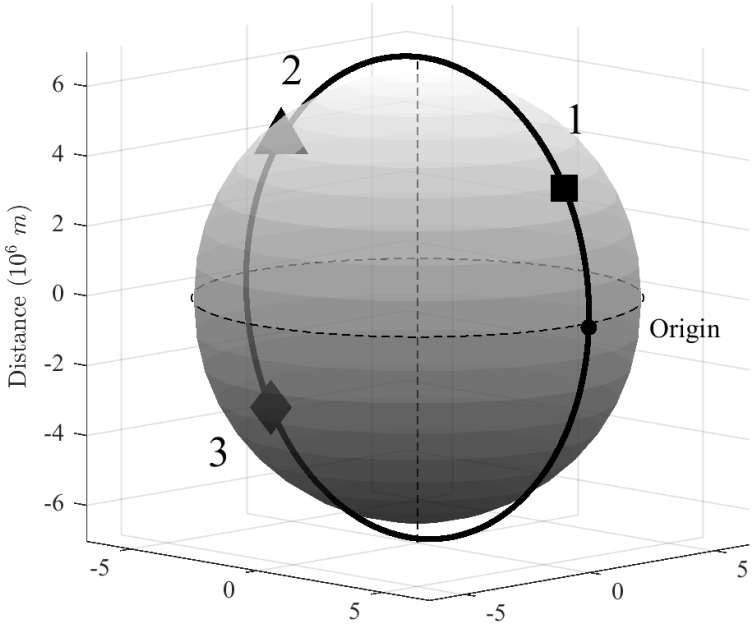

FIGURE 6.6: Location of Three Optimally Placed Thruster Instances

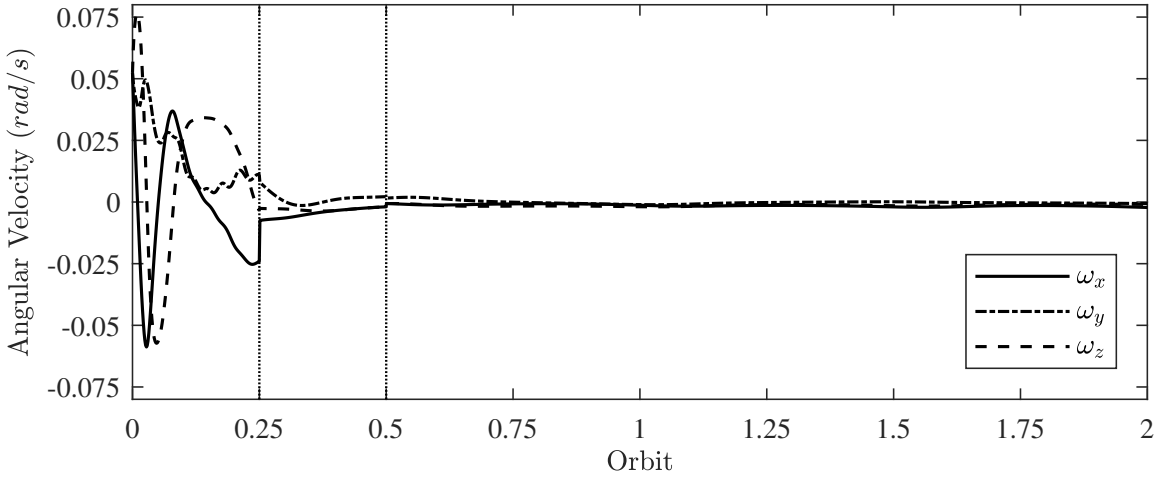

FIGURE 6.7: Hybrid Controller Utilizing 2 Arbitrarily Placed Thruster Instances

6.2.3 Altitude Variation

When comparing the performance of the B-Dot controller at 450km and 1350km it is apparent that the higher altitude does inhibit controller performance as seen by the metrics of table 6.3. This is because the tilted dipole moment we are using decreases by a factor or $R^{-3/2}$ as the distance from earth increases. The smaller the magnetic field, the smaller the possible magnetic torque can be applied to the spacecraft. Despite this however we see that the B-Dot controller is robust enough to function at the low and middle levels of low earth orbits where the majority of small spacecraft like the one modelled reside. We may infer from the factor that decreases the magnetic field over

distances $R^{-3/2}$, that due to the almost square nature of the factor the B-Dot algorithm may begin to fail at the highest levels of low earth orbits.

Examining the effect of the higher orbit on the optimal controller reveals that it is vastly more robust than the B-Dot controller at being capable of functioning at higher earth orbits. It is clear that like the B-Dot controller, it also suffers from the decreasing magnetic field as seen by the decreased level of momentum dampening before the impulse instance as compared to the 450 km orbit from figure 6.1. The robustness then comes from the impulsive part of the controller is able to compensate enormously when it is applied. This suggests that although optimal thruster instance selection from section 5.3 does not severely impact the performance of the hybrid controller at the lowest levels of low earth orbits, the effect might begin to be appear more pronounced as pure magnetic controllers experience higher levels of uncontrollability.

TABLE 6.3: Performance Metrics for B-Dot Controller at Differing Altitude Orbits

Figure	**Controller**	**Altitude** (km)	$\|\|\boldsymbol{\omega}\|\|$ $(\frac{rad}{s})$	$\|\|\boldsymbol{m}\|\|$ (Am^2)	**E** (GJ)
6.1	B-Dot	450	0.085	3.0	46.4
6.8	B-Dot	1350	0.092	2.8	49.2

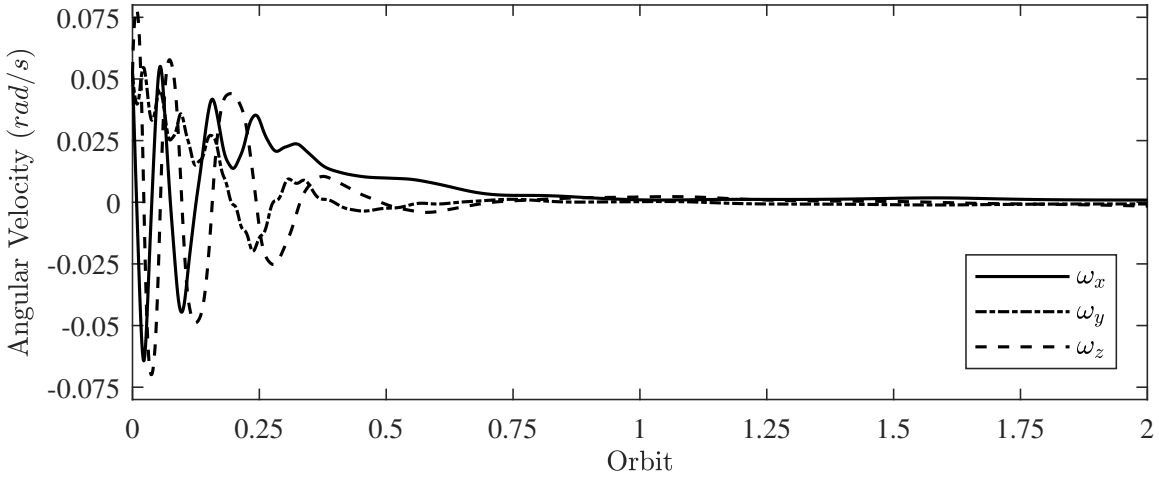

FIGURE 6.8: B-Dot Controller at 1350km Orbit

TABLE 6.4: Performance Metrics for Hybrid Controller at Differing Altitude Orbits

Figure	**Controller**	**Altitude** (km)	$\|\|\boldsymbol{\omega}\|\|$ $(\frac{rad}{s})$	$\|\|\boldsymbol{m}\|\|$ (Am^2)	**E** (GJ)
6.2	Hybrid	450	0.069	2.7	36.6
6.9	Hybrid	1350	0.068	2.5	39.6

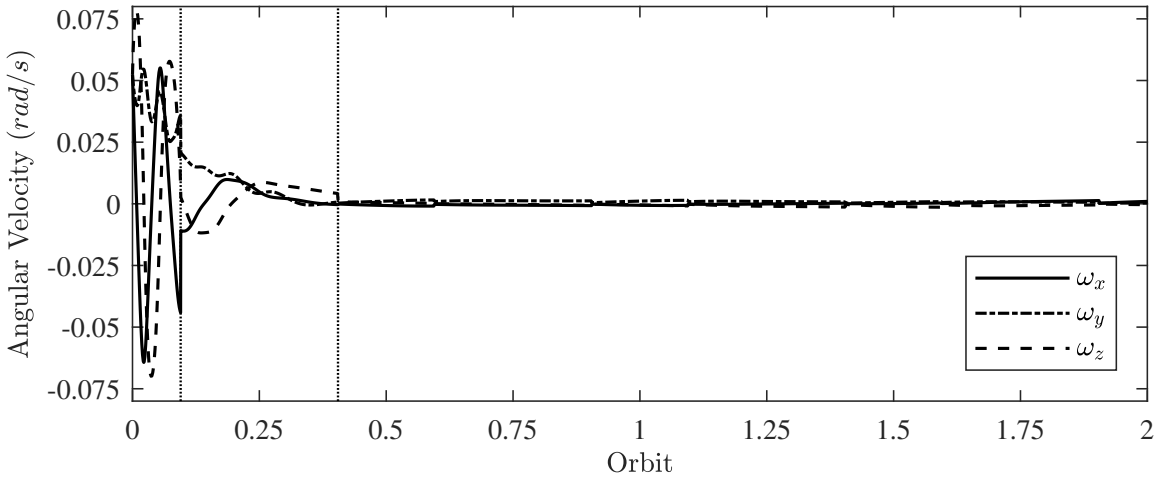

FIGURE 6.9: Hybrid Controller at 1350km Orbit

Chapter 7

Conclusion

7.1 Closing Thoughts

Ultimately the question of whether or not it is recommended to implement a B-Dot detumbling controller over an optimal hybrid controller or vice versa comes down to the system requirements. If there is an explicit requirement for the spacecraft to dump momentum as fast as possible in order to start active maneuvers then it is clear that the hybrid controller is much faster than the B-Dot controller. Such a case might arise when dealing with spacecraft at rapidly decaying low orbits which need to maximize their useful life time, or with regards to constellations of spacecraft requiring strict control with minimal downtime. However, if detumbling rates in the order of one orbit can be tolerated then there is no need to utilize a hybrid controller that favors speed.

The B-Dot controller appeared to work well for lower level, low earth orbits and was able to effectively dump momentum in about one orbital period. However as altitude increased, there was rapid performance degradation because the controller relies on a strong magnetic field. This proved the controller was not robust enough to readily handle various missions without the careful optimization. Although it wasn't tested it is assumed that due to the weaker, slowly changing magnetic field near the equator, the controller would not perform well under such conditions. For the common, near-polar, 87° orbits at altitudes of approximately 450 km, the B-Dot controller is expected to work reasonably well if detumbling times in the order of one orbital period are acceptable. For other cases, either different inclinations, or different altitudes the optimal hybrid controller should be considered.

Mission guarantee success should always be considered when choosing attitude controllers. The hybrid controller requires a thruster system, a working IMU as well as

computational resources in order to perform the necessary calculations and simulations ahead of launch. If these resources are not readily available or are not able to perform the necessary tasks in an expert manner, the whole mission success could be placed in jeopardy. Given that the momentum dumping procedure is mission critical as it may occur when not all the spacecraft's systems are online then the optimal control law may not even be an option because of the high number of systems it requires be operated.

If the benefits of a hybrid controller end up outweighing the potential risks, then it is clear no more than 2 impulse instants need be applied in order to rapidly bring the system to equilibrium. If the system is to be considered for higher than low level, low earth orbits, or if the orbit inclination is significantly different than 87 degrees then it is recommended a study of the optimal impulse firing times be performed, as the effect of choosing an optimal firing time became increasingly apparent for further from nominal conditions.

7.2 Future Work

There are a number of areas for future work as it relates to this project. A full characterization of the efficacy of the two controllers for all inclination angles and orbital altitudes need be performed in order to determine the performance of the two systems in less than optimal conditions. There appears to be no consensus on designing an optimal firing time algorithm for hybrid control systems similar to this as the theories surrounding these controllers are still quite new, thus innovative work could be done in this area. In addition, advanced methods for automatic tuning of the algorithm weight matrices would benefit designers and speed up mission analysis.

7.3 Summary

A simulator capable of modelling the kinematics and dynamics of a spacecraft was constructed inside Matlab for the purpose of testing the efficacy of detumbling algorithms for different input conditions. It was shown that both the B-Dot and Hybrid controllers performed reasonably well at a common used orbital altitude and inclination. As the orbit began to deviate from this the performance of the B-Dot controller began to degrade rapidly whereas the optimal controller was able to continue performing reasonably well.

Bibliography

[1] Ninfa Radicella, Gaetano Lambiase, Luca Parisi, and Gaetano Vilasi. Constraints on covariant horava-lifshitz gravity from frame-dragging experiment. 08 2014.

[2] Christopher J. Damaren Behrad Vatankhahghadim. Optimal combination of magnetic attitude control with impulsive thrusting. *Journal of Guidance, Control, and Dynamics*, 2016. URL `https://doi.org/10.2514/1.G001664`.

[3] Christopher J. Damaren James Richard Forbes. Linear time-varying passivity-based attitude control employing magnetic and mechanical actuation. *Journal of Guidance, Control, and Dynamics*, 2011. URL `https://doi.org/10.2514/1.51899`.

[4] Christopher J. Damaren Behrad Vatankhahghadim. Magnetic attitude control with impulsive thrusting using the hybrid passivity theorem. *Journal of Guidance, Control, and Dynamics*, 2017. URL `https://doi.org/10.2514/1.G002375`.

[5] Christopher J. Damaren Ludwik A Sobiesiak. Optimal continuous/impulsive control for lorentz-augmented spacecraft formations. *Journal of Guidance, Control, and Dynamics*, 2014. URL `https://doi.org/10.2514/1.G000334`.

[6] M. Lovera. Magnetic satellite detumbling: The b-dot algorithm revisited. In *2015 American Control Conference (ACC)*, pages 1867–1872, July 2015. doi: 10.1109/ACC.2015.7171005.

[7] Kevin Lee. Celestial equatorial coordinate system. URL `http://astro.unl.edu/naap/motion1/cec_units.html`.

[8] H. Alfven and C. G. Falthammar. Cosmical electrodynamics: Fundamental principles. *Oxford Univ. Press*, 1963.

[9] C.T. Russell. Geophysical coordinate transformations. *Cosmic Electrodynamics*, 2: 184–196, 1971.

[10] R. Mukundan. Quaternions: From classical mechanics to computer graphics, and beyond. URL `https://pdfs.semanticscholar.org/64e1/52a06f51f2d729e803c3e8c88f497a51a4aa.pdf`.

[11] C J Damaren. Hybrid magnetic attitude control gain selection. *Proceedings of the Institution of Mechanical Engineers, Part G: Journal of Aerospace Engineering*, 223 (8):1041–1047, 2009. doi: 10.1243/09544100JAERO641. URL https://doi.org/10.1243/09544100JAERO641.

[12] Mogens Blanke Wiśniewski, Rafał. Fully magnetic attitude control for spacecraft subject to gravity gradient. *Automatica*, 1999. doi: 10.1016/S0005-1098(99)00021-7.

[13] Space Flight Laboratory. Products services: Satellite platforms. URL https://www.utias-sfl.net/?page_id=89.

[14] Christopher J. Damaren. Rigid spacecraft attitude control. URL http://arrow.utias.utoronto.ca/~damaren/s3.pdf.

[15] Andras Varga Tiziano Pulecchi, Marco Lovera. Classical vs modern magnetic attitude control design: A case study. URL https://pdfs.semanticscholar.org/590c/6f98710cd4626b1f16ac97dc210fa0385747.pdf.

[16] F. L. Cortesi, T. H. Summers, and J. Lygeros. Submodularity of energy related controllability metrics. In *53rd IEEE Conference on Decision and Control*, pages 2883–2888, Dec 2014. doi: 10.1109/CDC.2014.7039832.

[17] Amos Ron. Numerical solution of differential equations - error analysis. URL http://pages.cs.wisc.edu/~amos/412/lecture-notes/lecture25.pdf.

[18] Devon Sanders Pedro A. Capo-Lugo, John Rakoczy. The b-dot earth average magnetic field. URL https://ntrs.nasa.gov/archive/nasa/casi.ntrs.nasa.gov/20140016484.pdf.